A scalar Poincaré map for struggling in *Xenopus* tadpoles

Mark Olenik[1*]

[1] *School of Biological Sciences, University of Bristol, Bristol BS81TQ, United Kingdom*

Conor Houghton[2]

[2] *School of Computer Science, Electrical and Electronic Engineering, and Engineering Mathematics, University of Bristol, Bristol BS81UB, United Kingdom*

Abstract

Short-term synaptic plasticity is widely found in many areas of the central nervous system. In particular, it is believed that synaptic depression can act as a mechanism to allow simple networks to generate a range of different firing patterns. The locomotor circuit of hatchling *Xenopus* tadpoles produces two types of behaviours: swimming and the slower, stronger struggling movement that is associated with rhythmic bends of the whole body. Struggling is accompanied by anti-phase bursts in neurons on each side of the spinal cord and is believed to be governed by a short-term synaptic depression of commissural inhibition. To better understand burst generation in struggling, we study a minimal network of two neurons coupled through depressing inhibitory synapses. Depending on the strength of the synaptic

*Corresponding author

Email addresses: `m.olenik@bristol.ac.uk` (Mark Olenik[1]), `conor.houghton@bristol.ac.uk` (Conor Houghton[2])

conductance between the two neurons, such a network can produce symmetric $n-n$ anti-phase bursts, where neurons fire n spikes in alternation, with the period of such solutions increasing with the strength of the synaptic conductance. Relying on the timescale disparity in the model, we reduce the eight-dimensional network equations to a fully explicit scalar Poincaré burst map. This map tracks the state of synaptic depression from one burst to the next, and captures the complex bursting dynamics of the network. Fixed points of this map are associated with stable burst solutions of the full network model, and are created through fold bifurcations of maps. We derive conditions that describe period increment bifurcations between stable $n-n$ and $(n+1)-(n+1)$ bursts, producing a full bifurcation diagram of the burst cycle period. Predictions of the Poincaré map fit excellently with numerical simulations of the full network model, and allow the study of parameter sensitivity for rhythm generation.

Keywords: *Xenopus*, Synaptic depression, Poincaré map, Dynamical system, Neuronal bursting

---

1. Introduction

Short-term synaptic plasticity may have a role in burst activity in central pattern generators (CPGs). Short-term synaptic depression is commonly found in neuronal networks involved in the generation of rhythmic movements, such as in the pyloric CPG of the spiny lobster (Manor et al., 1997; Rabbah & Nadim, 2007), or in the lumbosacral cord of the chick em-

bryo (Donovan et al., 1998). Synaptic depression modulates the strength of synapses in response to changes to the presynaptic firing frequency. At a high neuronal firing frequency, depression weakens the strength of synapses and therefore reduces the magnitude of the respective postsynaptic response. At low firing frequency, it allows sufficient time for the synapse to recover from depression between spikes, leading to a stronger postsynaptic response. In reciprocal networks, synaptic depression has been shown to act as a "switch", giving rise to a wide range of network dynamics such as synchronous and multi-stable rhythms, as well as fine tuning the frequency of network oscillations (Nadim & Manor, 2000; Nadim et al., 1999; Bose & Booth, 2011).

A switch between two CPG rhythms that is believed to be guided by synaptic depression can be observed in hatchling *Xenopus* tadpoles. Tadpoles select between two main behaviours in response to different types of skin stimuli. Swimming occurs in response to a brief touch or a single electrical pulse to the trunk (Clarke et al., 1984), and is accompanied by 12 to 25 Hz alternating left and right bending moves (Kahn et al., 1982). Alternatively if held, tadpoles produce struggling, with stronger, slower 2 to 10 Hz bending moves of the whole body (Kahn & Roberts, 1982). The switch from swimming to struggling is associated with a change from a pattern of low-frequency alternating single spikes in swimming (Kahn et al., 1982), to one of alternating high-frequency bursting in struggling (Kahn & Roberts, 1982; Soffe, 1993). Both swimming and struggling are thought to be produced by two overlapping spinal cord CPG networks that share some types

of individual neurons. One such shared class of neurons are the inhibitory commissural interneurons (cINs), which have reciprocal depressing inhibitory synapses with neurons on the opposite site of the spinal cord (Li et al., 2007).

Brown (1911) pioneered the idea that synaptic depression acts as a burst termination mechanism in reciprocally inhibitory CPGs involved in rhythm generation of locomotion. Weakening of inhibition as a result of synaptic depression allows the antagonistic side to be released, start firing, and terminate the ongoing burst. Brown's rhythmogenesis hypothesis has been considered one of a handful of standard mechanisms for generating locomotion rhythms in vertebrates (Reiss, 1962; Perkel & Mulloney, 1974; Friesen, 1994). Brown's hypothesis is also believed to explain struggling in tadpoles (Li et al., 2007), where the periodic weakening of antagonistic cIN inhibition through short term synaptic depression may act as a burst termination mechanism that produces the antiphase burst rhythm.

Here we study Brown's rhythmogenesis hypothesis and the mechanisms of burst generation in struggling using a generic half-centre CPG that consists of two identical, tonically active Morris-Lecar (Morris & Lecar, 1981) neurons that are coupled through inhibitory depressing synapses. Each neuron represents a population of cINs on either side of the tadpole spinal cord. Our model reduction is based on the approach previously taken by Bose & Booth (2011), where the dynamics of a similar two-cell reciprocal inhibitory network with depression has been analysed. Bose & Booth's numerical simulations showed that when the reciprocal synaptic conductance between the two neu-

rons was varied, the model produces symmetric $n-n$ anti-phase bursts, with stronger synaptic coupling leading to longer bursts (see fig. 3). Bose & Booth used methods from geometric singular perturbation theory to separate the timescales of the fast membrane, and the slow synaptic dynamics of the network and derive one-dimensional conditions for the existence of stable $n-n$ solutions (for $n < 3$). Most importantly, they showed that the type of pattern largely depends on the slow depression dynamics of the synapses between the two neurons, and can therefore be predicted by knowing the strengths of the synaptic conductances of the two synapses.

In this work we extend the analysis by Bose & Booth (2011) by reducing a two-cell model to a scalar Poincaré map that tracks the evolution of the depression from the beginning of one burst to the beginning of the next burst. Fixed points of our map are associated with stable $n-n$ burst solutions. Our map construction is motivated by the burst length map of a T-type calcium current, utilised in Matveev et al. (2007), which approximates the anti-phase bursting dynamics of a network of two coupled Morris-Lecar neurons. In contrast to our model, the Matveev et al. network does not contain short-term synaptic depression, and burst termination is instead accomplished through the dynamics of a slow T-type calcium current.

Our Poincaré map replicates the results from numerical simulations of the full two-cell ODE system: Given the strength of maximum conductance between the two neurons, fixed points of our map predict the type and period of $n-n$ patterns, the switch between burst solutions of different periods, as

well as the occurrence of co-existent solutions. We show that fixed points are created via a fold bifurcation of maps, and we derive algebraic conditions that predict the period increment bifurcations that allow the switch between $n - n$ and $(n + 1) - (n + 1)$ solutions. Because our map is fully explicit, it lays the framework for studying the effects of any other model parameter on network dynamics without the need to run expensive numerical integrations of the ODEs. Our analysis suggests that understanding the dynamics of the slow depression is sufficient to explain the generation of burst solutions in the tadpole struggling network.

This paper is organised as follows. First, we introduce the network of two neurons, and describe the properties of single cell and synapse dynamics. We use numerical simulations of the network to provide an intuition for the range of possible burst dynamics the system can produce. Next, we state and justify the simplifying assumptions that are necessary for the map construction. Finally, we analytically derive the first return map of the depression variable as well as the conditions that are required for stable solutions to bifurcate between $n - n$ and $(n + 1) - (n + 1)$ solutions. We end this work with a discussion.

2. Model

We consider a pair of identical Morris-Lecar neurons (Morris & Lecar, 1981), with parameters adapted from Bose & Booth (2011). The Morris-Lecar model is a set of two first-order differential equations that describe the

membrane dynamics of a spiking neuron. The depolarisation is modelled by an instantaneous calcium current, and the hyperpolarisation by a slow potassium current and a leak current. The membrane potential v_i and potassium activation w_i of neuron i $(i, j = 1, 2)$ is described by:

$$\dot{v}_i = f(v_i, w_i) - \bar{g} s_j (v_i - v_s), \tag{1}$$

$$\dot{w}_i = h(v_i, w_i). \tag{2}$$

Here v_s is the inhibitory reversal potential, and $\bar{g}$ and s_j are the maximal synaptic conductance and the synaptic gating, respectively, constituting the total inhibitory conductance $\bar{g} s_j$ from neuron j to neuron i. Function $f(v_i, w_i)$ describes the membrane currents of a single cell:

$$f(v_i, w_i) = -g_{\mathrm{Ca}} m_\infty(v_i)(v_i - v_{\mathrm{Ca}}) - g_{\mathrm{K}} w_i (v_i - v_{\mathrm{K}}) - g_{\mathrm{L}}(v_i - v_{\mathrm{L}}) + I. \tag{3}$$

The currents include a constant current I, and three ionic currents: an instantaneous calcium current, a potassium current, and a leak current, with respective reversal potentials v_{Ca}, v_{K}, and v_{L}, as well as maximum conductances g_{Ca}, g_{K}, and g_{L}. The function $h(v_i, w_i)$ models the kinetics of the potassium gating variable w_i, and is given by

$$h(v_i, w_i) = \frac{w_\infty(v_i) - w_i}{\tau_w} \ . \tag{4}$$

The steady-state activation functions m_∞ and w_∞ as well as the default model parameters are described in Appendix A.

The dynamics of the synaptic interactions between the neurons are governed by a synaptic gating variable s_i and a depression variable d_i:

$$\dot{s}_i = -s_i/\tau_s \ , \tag{5}$$

$$\dot{d}_i = (1 - d_i)/\tau_d \ . \tag{6}$$

Variable d_i describes a firing rate dependent depletion mechanism that governs the amount of depression acting on the synapse. Our model is agnostic with respect to the exact mechanism of this depletion, be it pre- or post-synaptic. In between spikes s_i decays with time constant τ_s, while d_i recovers with time constant τ_d. Because synaptic depression occurs on a much slower timescale than synaptic inhibition, we assume $\tau_d \gg \tau_s$. At spike time when the voltage v_i crosses a synaptic threshold v_θ, the synaptic variable s_i is reset to the current value of d_i, and d_i is scaled down by the depression strength parameter λ, where $0 < \lambda < 1$. This results in the following discontinuous reset rule on spike time:

$$s_i \leftarrow d_i \ , \tag{7}$$

$$d_i \leftarrow \lambda d_i \ . \tag{8}$$

The equations for the depression model were adapted from Bose et al. (2001).

These equations are a mathematically tractable simplification of the established phenomenological depression model previously described by Tsodyks & Markram (1997). The original equations in Bose et al. include an exponential decay of d_i throughout the active phase of the action potential, that is $\dot{d}_i = -d_i/\tau_\beta$ for $v_i > v_\theta$. To simplify the mathematical analysis we have reduced these dynamics to a single-reset event at spike time according to eq. (8). This simplification is natural given an approximately constant duration of the active phase of an action potential, and it will become evident from our results that this simplification does not qualitatively change the dynamics of the network compared to Bose et al.'s original equations, where depression dynamics are described by an exponential decay.

When the cells are uncoupled ($\bar{g} = 0$), the membrane dynamics are determined by the cubic v-nullcline $v_\infty(v_i)$ and the sigmoid w-nullcline $w_\infty(v_i)$, satisfying $\dot{v}_i = 0$ and $\dot{w}_i = 0$, respectively. The two curves intersect along the middle branch of v_∞, creating an unstable fixed point $p_f = (v_f, w_f)$ with a surrounding stable limit cycle of period T (fig. 1A). Trajectories along that limit cycle have the familiar shape of the action potential (fig. 1B). The trajectory of an action potential can be dissected into four phases: (1) a silent phase, (2) a jump up, (3) an active phase, and (4) a jump down (see e.g. Ermentrout & Terman, 2010). During the silent phase the trajectory evolves along the left branch ($v_i < v_\theta$) of the cubic v-nullcline. Once the trajectory reaches the local minimum of v_∞, it "jumps up" to the right branch ($v_i > v_\theta$), crossing the firing threshold v_θ. During the active phase the tra-

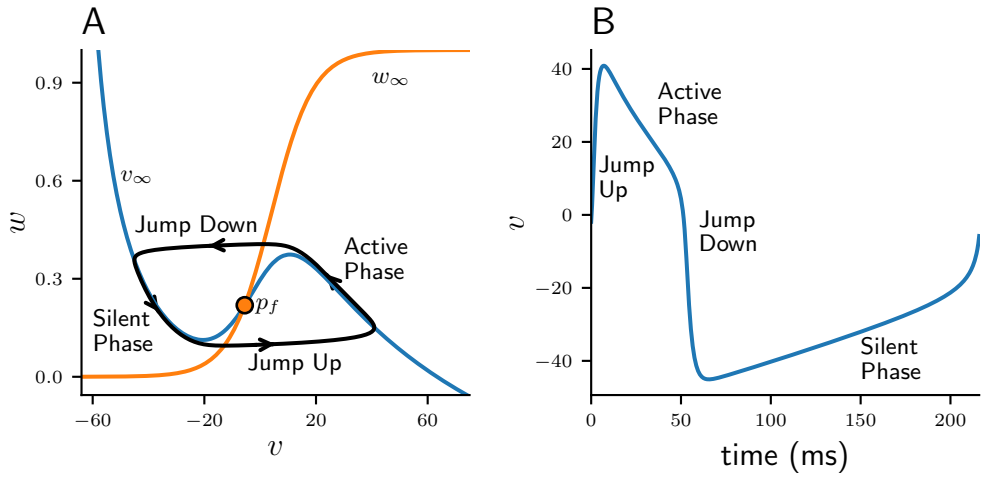

Figure 1: Periodic solution of relaxation-oscillator model neuron. **A**: Projection of limit cycle onto (v, w)-phase plane with v-nullcline (blue, v_∞) and w-nullcline (orange, w_∞). Unstable fixed point p_f is indicated by an orange dot. **B**: Corresponding voltage trace $v(t)$ of an action potential.

jectory then evolves along the right branch of the cubic until it arrives at the local maximum, where it "jumps down" to the left branch commencing a new cycle.

The two-cell network model is numerically integrated using an adaptive step-size integrator for stiff differential equations implemented with XPPAUT (Ermentrout, 2002) and controlled through the Python packages SciPy (Virtanen et al., 2020) and PyXPP (Olenik, 2021). The following mathematical analysis is performed on the equations of a single cell. Unless required for clarity, we will therefore omit the subscripts i, j from here on.

3. Results

3.1. Anti-phase burst solutions

Short-term synaptic depression of inhibition in a half-centre oscillator acts as a *burst termination* mechanism (Brown, 1911) and is known to produce $n - n$ anti-phase burst solutions of varying period. Such $n - n$ solutions consist of cells firing bursts of n spikes in alternation. Figure 2A shows a typical $4 - 4$ burst. While one cell is firing a burst it provides an inhibitory conductance to the other cell, preventing it from firing. Therefore, at any given moment one cell is spiking while the other is inhibited. Consistent with Bose & Booth (2011) we will refer to the currently firing cell as "free" and we will call the inhibited cell "quiet". Additionally, we will distinguish between two phases of a $n - n$ solution: We will refer to the burst duration of a cell as the "free phase", which is the time between the first spike and the last spike in a burst. And we will call the remaining duration of a cycle, when a cell is not spiking, the "quiet phase".

With each action potential of the free cell, short-term depression leads to a step-wise decrease of d, and consequently of s (fig. 2B). If d depresses faster at spike time than it can recover in the inter-spike-intervals (ISIs), the total synaptic conductance $\bar{g}s$ will eventually become sufficiently small to allow for the quiet cell to be released and start firing, thus inhibiting the previously free cell. While a cell is quiet its depression variable can recover. Once the quiet cell becomes free again its synaptic inhibition will be sufficient to terminate the burst of the previously free cell and commence a new cycle. As previously

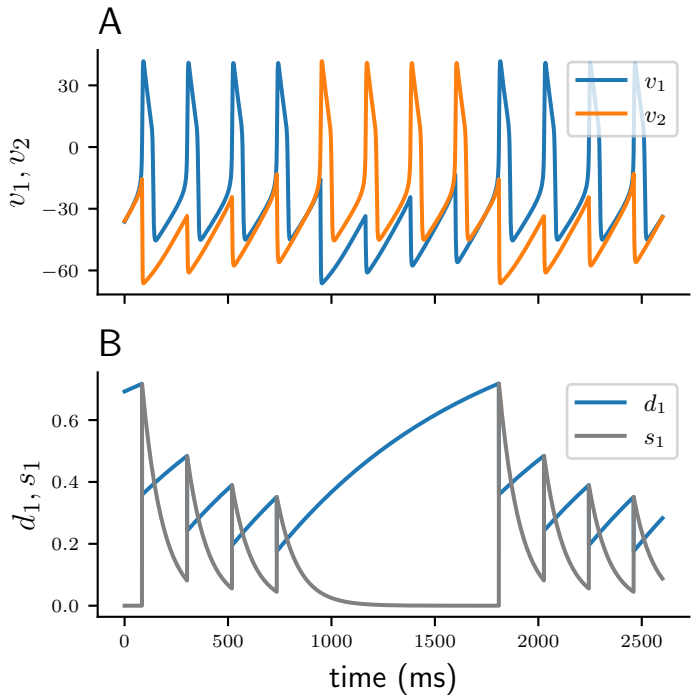

Figure 2: Solution profiles of a $4-4$ burst. **A**: Membrane potentials of cell 1 (v_1, blue), and cell 2 (v_2, orange). **B**: Synaptic variables d_1 (blue) and s_1 (grey) of cell 1.

demonstrated by Bose & Booth (2011), in a two-cell reciprocally inhibitory network with synaptic depression the coupling strength $\bar{g}$ determines the type of $n-n$ solution. Increasing $\bar{g}$ produces higher $n-n$ burst solutions with more spikes per burst and a longer cycle period. Figure 3 shows numerically stable $n-n$ solutions for varying values of $\bar{g}$. For small values of $\bar{g}$ the network produces anti-phase spiking $1-1$ solutions. As $\bar{g}$ is increased the network generates solutions of increasing n, that is $2-2$, $3-3$, and $4-4$. When $\bar{g}$ is sufficiently large (bottom of fig. 3), one of the cells continuously spikes at its uncoupled period T while the other cell remains fully suppressed.

Depending on the initial conditions either of the two cells can become the suppressed cell, which is why the suppressed solution is numerically bistable.

Branches of numerically stable $n-n$ solutions and their associated limit cycle period for varying values of $\bar{g}$ are depicted in fig. 4A (see appendix Appendix B for algorithm description). Not only do higher $n-n$ solutions branches require stronger coupling $\bar{g}$, but also within $n-n$ branches the period increases with $\bar{g}$. In line with Bose & Booth (2011) we find small overlaps between solution branches indicating numerical bistability, for example such as between the $2-2$ and $3-3$ solution branches. Branches of higher $n-n$ burst solutions occur on increasingly smaller intervals of $\bar{g}$, for instance is the $\bar{g}$ interval of the $5-5$ branch shorter than that of the $4-4$ branch. The interval between the $5-5$ branch and the suppressed solution (region between dotted lines in fig. 4A) not only contains even higher numerically stable $n-n$ solutions, such as $11-11$ bursts, but also other non-symmetric $n-m$ solutions as well irregular, non-periodic solutions. However, the analysis in the following sections will only be concerned with the numerically stable and symmetric $n-n$ solutions.

3.2. Mathematical analysis of two-cell network

The goal of the following mathematical analysis is to reduce the complexity of the eight-dimensional system to some easily tractable quantity. As we will see later this quantity is the value of the depression variable d of either of the two cells. We will construct the solution of d in a piecewise man-

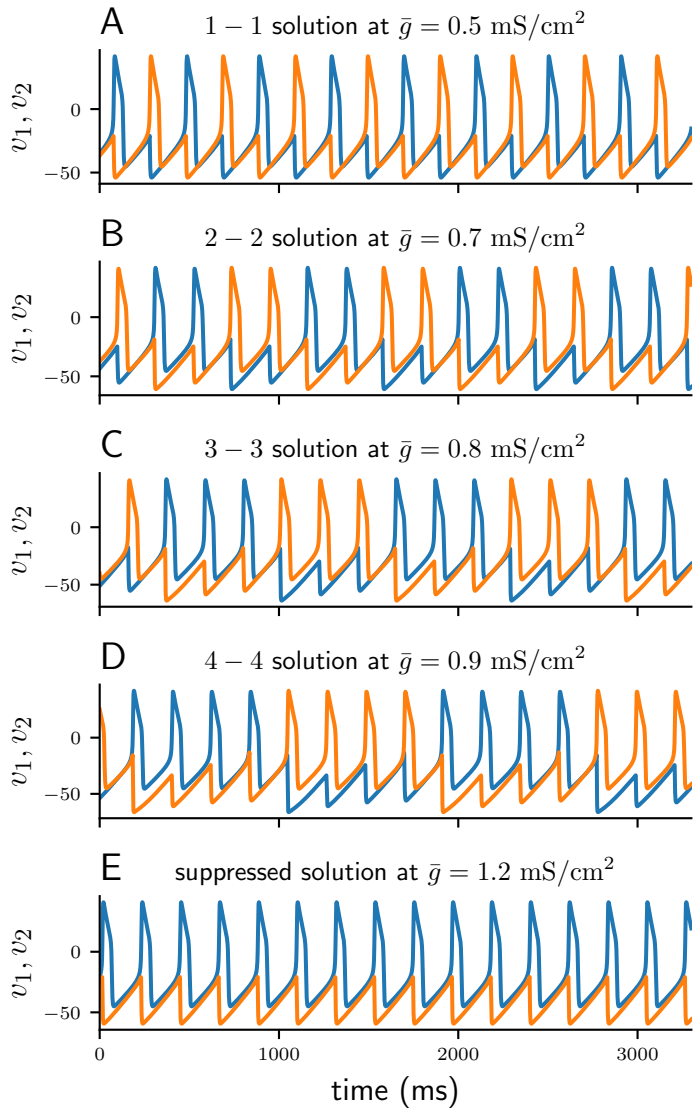

Figure 3: Voltage traces of numerically stable solutions for increasing values of the coupling strength $\bar{g}$ (increasing top to bottom).

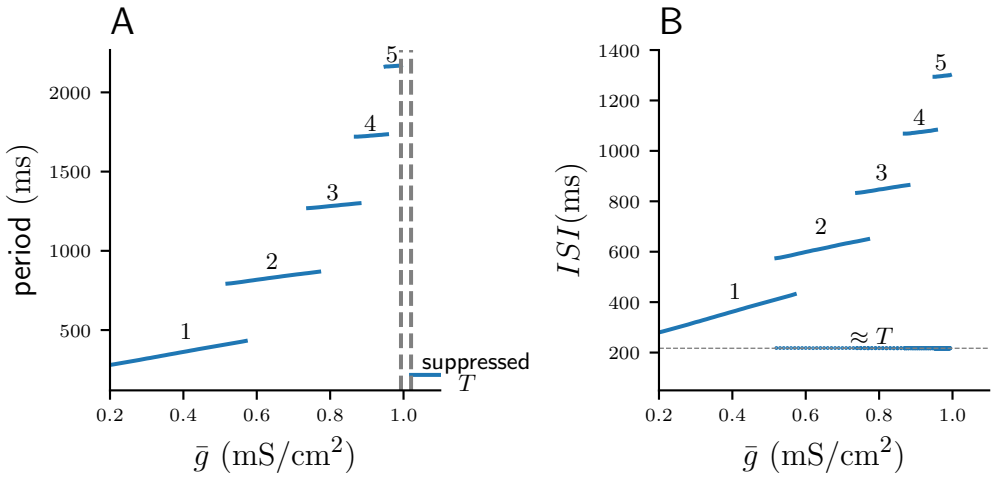

Figure 4: Numerically computed bifurcation diagrams of stable $n-n$ solutions for increasing coupling strength $\bar{g}$. **A**: Period of stable solutions. Dashed lines show the interval between the $5-5$ and the suppressed solutions, where higher period $n-n$ solutions occur on increasingly smaller intervals of $\bar{g}$. **B**: ISIs corresponding to $n-n$ solutions in A. Long ISIs are associated with the quiet phase of a burst, short ISIs with the free phase. During the free phase, ISIs are of approximately constant duration T.

ner from one spike to the next, first during the free phase, and then during the quiet phase. This construction will require two assumptions about the membrane and synaptic dynamics. The first assumption states that during a burst the free cell fires at its uncoupled period T, which allows us to build the solution of d during the free phase. The second assumption states that once the inhibitory conductance acting on the quiet cell drops below a critical threshold, the cell is immediately released and fires. The second assumption is necessary to predict the release time of the quiet cell, which allows us to model the recovery of d during the quiet phase. In other words, the second assumption requires that the release of the quiet cell from inhibition depends

only on the timecourse of the inhibition, and not on the membrane dynamics of the quiet cell. Both assumptions can be observed in coupled relaxation-oscillator types of neurons such as the Morris-Lecar model we use, and will be numerically verified below. Both assumptions were first explored in Bose & Booth (2011) to derive algebraic conditions that guarantee the periodicity of the depression variable for different $n-n$ solutions. However here we will use these assumptions to construct a Poincaré map of d, which will provide a geometric intuition for the dynamics of the full two-cell network and its dependence on model parameters.

Our first assumption about the model states that the free cell fires at its uncoupled period T, that is, during the free phase of a burst we have $ISI = T$. Solution profiles in fig. 3 suggest that the ISIs in the free phase are indeed approximately constant. We can further numerically confirm this observation by capturing the ISIs of the stable solutions from the bifurcation diagram in fig. 4A. Figure 4B shows two types of ISIs as $\bar{g}$ is varied, long ISIs and short ISIs. Long ISIs lie on multiple branches, each branch associated with a stable $n-n$ solution, and are monotonically increasing with $\bar{g}$. These ISIs lie in the quite phase of the burst, and thus correspond to the time interval between the last spike time of a burst, and the full cycle period. The short ISIs are calculated from the spikes within the free phase and do not vary significantly with $\bar{g}$, but are approximately $ISI \approx T$, affirming our first assumption. Assuming $ISI = T$ allows us to ignore the non-linear membrane dynamics during the free phase, and to construct the evolution of

the synaptic variables iteratively from spike to spike. Assuming $ISI = T$ in the free phase seems reasonable given that inhibition acting on the quiet cell decays exponentially to zero on a much shorter timescale than the duration of the ISI, and therefore, once the quiet cell is released its trajectory quickly approaches the spiking limit cycle.

Our second assumption states that the quiet cell is released and spikes as soon as inhibition from the free cell drops below a constant threshold. We will now define such a "release condition" by exploiting the discrepancy in timescales between the fast membrane dynamics, and the slower synaptic dynamics. Let us first consider the dynamics of a single Morris-Lecar neuron. We fix the synaptic variable that acts on the cell by setting $s = 1$, which also makes the applied synaptic conductance $\bar{g}s$ constant. Recall from fig. 1A that in case of a single uncoupled cell ($\bar{g}s = 0$), the v- and w-nullclines intersect at some unstable fixed point $p_f = (v_f, w_f)$, while trajectories revolve around a stable spiking limit cycle. Increasing $\bar{g}s$ moves the cubic v_∞ with the ensuing unstable fixed point p_f down the sigmoid w_∞ in the $(v - w)$-plane (fig. 5). When $\bar{g}s$ is large enough, the fixed point p_f becomes stable, attracting all previously periodic trajectories. There exists a unique value $\bar{g}s = g^\star$ when p_f changes stability and the stable limit cycle vanishes. Thus, when a constant inhibitory conductance is applied, $\bar{g}s < g^\star$ acts as a necessary condition for a cell to spike. In contrast, when $\bar{g}s > g^\star$ inhibition is strong enough to prevent a cell from spiking (Bose & Booth, 2011).

Now let us analyse the nullclines of the quiet cell when the two cells are

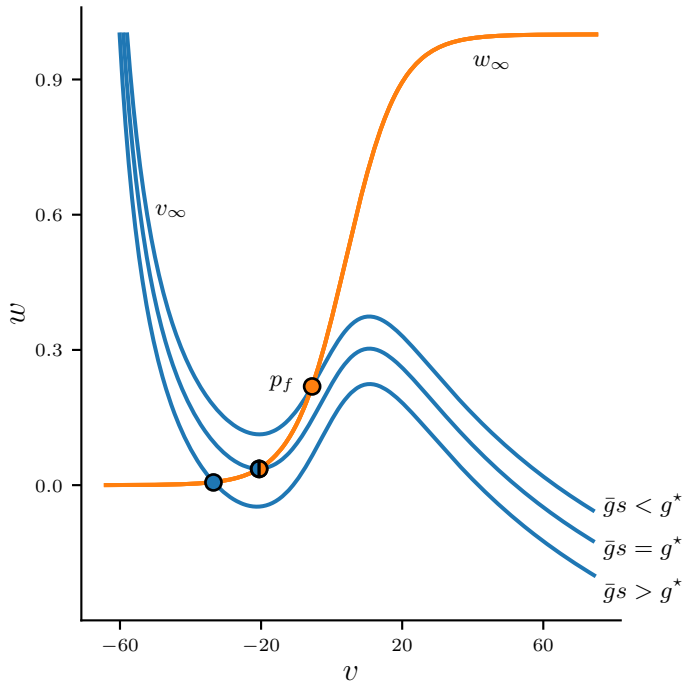

Figure 5: Nullclines v_∞ (blue) and w_∞ (orange) in the (v, w)-phase plane for different values of the total synaptic conductance $\bar{g}s$. For small $\bar{g}s < g^\star$, fixed point p_f is unstable (orange point). Larger values $\bar{g}s$ move v_∞ down in the (v, w)-plane until p_f changes stability (half orange, half blue point) at some critical total conductance value $\bar{g}s = g^\star$, and becomes stable (blue point) for $\bar{g} > g^\star$.

coupled via synaptic inhibition with depression. Let $\bar{g}s$ here denote the total synaptic conductance which acts on the quiet cell and is produced by the free cell, and let p_f be the fixed point associated with the quiet cell. At the start of the burst of the free cell we have $\bar{g}s > g^\star$ and p_f is stable. When the free cell spikes $\bar{g}s$ peaks (eq. (7)) and p_f jumps down the w-nullcline. Then in between spikes $\bar{g}s$ decays exponentially (eq. (5)) causing p_f to move up the w-nullcline while attracting trajectories of the quiet cell. Once depression

causes the synaptic conductance to become small enough to satisfy $\bar{g}s < g^\star$ and the quiet cell is released, fixed point p_f becomes unstable allowing the quiet cell to fire. If the trajectory of the quiet cell remains sufficiently close to p_f when it changes stability, then $\bar{g}s < g^\star$ acts as a release condition that is not only necessary, but also sufficient for firing of the quiet cell. In this case the release of the quiet cell occurs precisely when

$$\bar{g}s = g^\star \tag{9}$$

is satisfied.

Whether the (v, w)-trajectory of the quiet cell can remain close enough to p_f to make eq. (9) sufficient for firing depends largely on the coupling strength $\bar{g}$ and the timescale disparity between membrane dynamics and synaptic dynamics (Bose & Booth, 2011). It is straightforward to test our assumption of a release condition by numerically integrating the full system of ODEs and calculating the time interval between the first spike of the quiet cell and the time when $\bar{g}s$ first crosses $g^\star$. We will call this time interval the "release delay". If our assumption holds, we would expect an approximately zero release delay. Figure 6 shows the numerically computed graph of the release delay for varying $\bar{g}$. The graph shows three distinct branches, next to each branch we also plot the timecourse of a corresponding sample solution of the total synaptic conductance $\bar{g}s$ of both cells. For the rightmost branch where $\bar{g} > 0.592$ mS/cm^2 the release delay is approximately zero. Here the

first spike of the quiet cell can be accurately predicted by the release condition in eq. (9). The leftmost and middle branches for $\bar{g} < 0.592$ mS/cm^2 show a release delay greater than zero, the quiet cell does not immediately fire when the release condition is first satisfied, and eq. (9) does not accurately predict the release of the quiet cell. The leftmost and middle branches contain $1-1$ and $2-2$ solutions respectively. In both cases the coupling $\bar{g}$ is not sufficiently strong to allow trajectories of the quiet cell to be close enough to p_f to guarantee spiking once $\bar{g}$ crosses $g^\star$. Note that in the middle branch $\bar{g}s$ crosses $g^\star$ twice, and only after the second crossing does the quiet cell fire. The following map construction relies on the assumption that the release condition in eq. (9) can accurately predict the release time of the quiet cell. Given our model parameters this is only possible for sufficiently large $\bar{g} > 0.592$ mS/cm^2. For completeness, however, we will also consider values $\bar{g} < 0.592$ mS/cm^2 in the following analysis, bearing in mind that in this parameter range our map will not be accurate.

In summary: For $\bar{g} > 0.592$ mS/cm^2 the release condition is sufficient to predict when the quiet cell is released. Due to the symmetry of $n-n$ solutions the release occurs at exactly half the period of the full cycle, that is at $P/2$. The release time therefore uniquely determines the type of $n-n$ solution. Furthermore, computation of the release time does not depend on the membrane nor the synaptic dynamics of the quiet cell. Instead, the solution of the synaptic variable s of the free cell is sufficient to predict when $\bar{g}s = g^*$ is satisfied. Finally, s is solely determined by the evolution of the

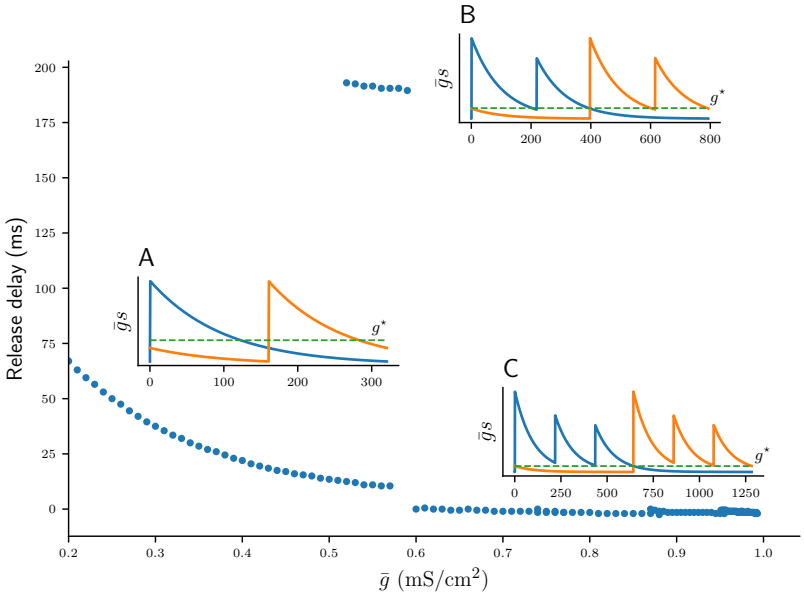

Figure 6: Numerically computed values of the release delay for varying $\bar{g}$. Each of the three branches (A, B, C) also shows the timecourse of the total synaptic conductance $\bar{g}s$ of a sample stable solution of both cells (blue and orange), as well as the release conductance $g^\star$ (dashed green line). **A**: Branch corresponding to the $1-1$ solution. Here the quiet cell only spikes after a significant release delay. **B**: Branch with a long release delay associated with a subset of $2-2$ solutions. Here the release condition is briefly satisfied after the first spike of cell 1. This does not cause firing of cell 2, which only occurs after the second spike of cell 1. **C**: Branch with $n-n$ solutions where release delay is approximately zero and the release condition is sufficient for firing of cell 2.

depression variable d of the free cell. Constructing a solution of d during the free phase of either cell will therefore uniquely determine the solution of the full eight-dimensional network. However, finding the solution d requires us to know the initial value $d(0)$ at the start of a cycle at $t = 0$. In the next section we will construct a scalar return map that tracks these initial values $d(0)$ from cycle to cycle of stable $n - n$ solutions.

3.3. Construction of the scalar Poincaré map Π_n

In this section we construct the scalar Poincaré map $\Pi_n : d^\star \mapsto d^\star$. Here the discrete variable $d^\star$ tracks the values of the continuous depression variable d at the beginning of each $n - n$ burst. The map Π_n therefore describes the evolution of d, of either of the two cells, from the beginning of one cycle to the beginning of the next cycle. To simplify the map construction we will assume that a free cell fires exactly n times before it becomes quiet. Later we will relax this assumption. We will construct Π_n by evolving d first during the free phase and then during the quiet phase of the $n-n$ limit cycle. First, let us give explicit definitions of the free and quiet phases. A schematic illustration of both phases is given in fig. 7.

Suppose that at $t = 0$ cell 1 becomes free with some initial $d(0)$. Cell 1 then fires n spikes at the uncoupled period T. Let $s(t)$ and $d(t)$ be the corresponding solutions of the synaptic and depression variables of cell 1. After n spikes the total conductance $\bar{g}s(t)$ acting on the quiet cell 2 has decayed sufficiently to satisfy the release condition (9), that is at some time

$t = (n-1)T + \Delta t$ we have $\bar{g}s(t) = g^\star$. Cell 2 is then released and prevents cell 1 from further spiking. Here Δt is the *inter-burst-interval*, or the time between the last spike of cell 1 and the first spike of cell 2 (Bose & Booth, 2011). Once released, cell 2 also fires n spikes until cell 1 becomes free once again at the cycle period. Let P_n denote the full cycle period of a $n-n$ solution:

$$P_n = 2(n-1)T + 2\Delta t. \tag{10}$$

We can now define the free and quiet phases of cell 1 explicitly. The free phase is the time interval between the first and last spikes of the burst, that is for time $0 < t < (n-1)T$. During the free phase of cell 1, the quiet cell 2 is inhibited sufficiently strong to prevent it from firing, hence $\bar{g}s > g^\star$. The quiet phase of cell 1 is the remaining duration of the cycle when the cell is not firing, that is for $(n-1)T < t < 2(n-1)T + 2\Delta t$.

Note that only the quiet phase depends on Δt, and Δt will play a central role in the construction of Π_n. From eq. (10) Δt can be be computed as

$$\Delta t = \frac{1}{2}P_n - (n-1)T. \tag{11}$$

We can use eq. (11) and the numerically computed bifurcation diagram of the period for stable $n-n$ solutions in fig. 4A to obtain the graph of Δt as a function of $\bar{g}$ (fig. 8). Each continuous branch of Δt is monotonically increasing and corresponds to a $n-n$ burst: Stronger coupling $\bar{g}$ increases the total synaptic conductance $\bar{g}s$ that acts on the quiet cell, thus delaying

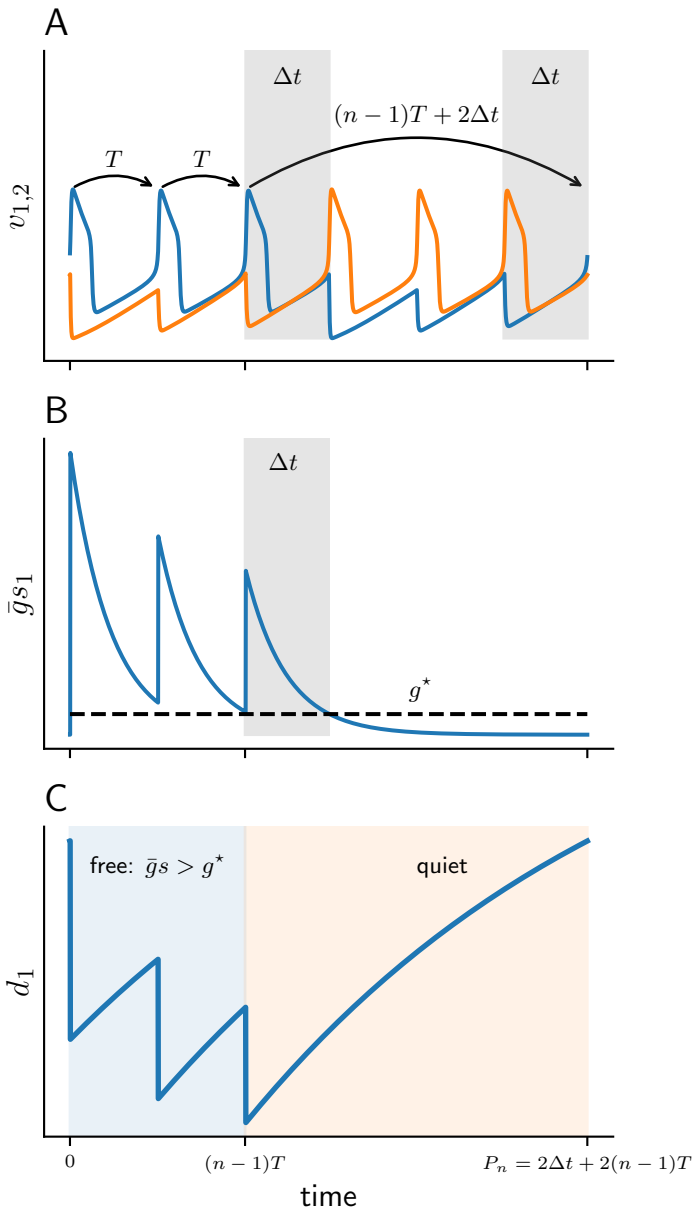

Figure 7: Schematic diagram of the free and quiet phases for a $3-3$ solution. **A**: Membrane potentials of cell 1 (v_1) and cell 2 (v_2). The grey patches depict inter-burst-intervals Δt. **B**: Total synaptic conductance of cell 1 ($\bar{g}s_1$) as it crosses the release conductance $g^\star$. **C**: Solution $d_1(t)$ of depression variable of cell 1, during free (blue) and quiet phases (orange).

its release. It is easy to see that for any n-branch we have $\Delta t < T$: Once Δt crosses T, the free cell can "squeeze in" an additional spike and the solutions bifurcate into a $(n+1)-(n+1)$ burst.

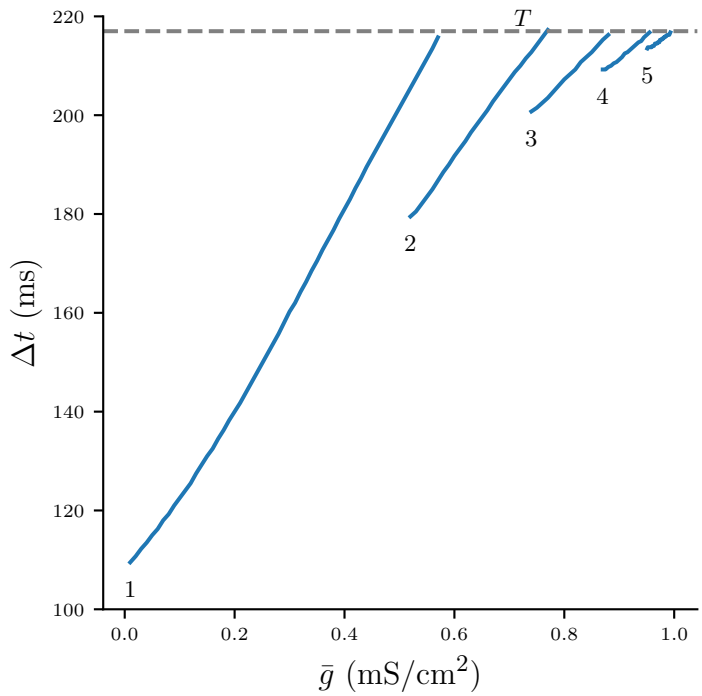

Figure 8: Numerically computed bifurcation diagram of Δt for varying $\bar{g}$. Each continuous branch is associated with a stable $n-n$ burst solution. Increasing $\bar{g}$ increases Δt until the solutions bifurcate at $\Delta t \approx T$.

Distinguishing between the free and quiet phases of a cycle allows us to describe the dynamics of the depression variable d explicitly for each phase. As can be seen from fig. 7C, during the free phase d depresses at spike times and recovers in the ISIs. In contrast, during the quiet phase d only recovers and does not depress. Given the initial $d^\star = d(0)$ at the beginning of the cycle and the number of spikes in the free phase n, we can now construct the

burst map Π_n. The map

$$\Pi_n(d^\star) = Q_n\big(F_n(d^\star)\big) \tag{12}$$

is a composition of two maps. Map

$$F_n : d^\star \mapsto \Delta t \tag{13}$$

models the evolution of d in the free phase. F_n takes an initial value $d^\star$ and calculates the inter-burst-interval Δt. Map

$$Q_n : \Delta t \mapsto d^\star \tag{14}$$

models the recovery of d in the quiet phase. Given some Δt map Q_n computes $d^\star$ at the start of the next cycle.

Our aim in the following analysis is to elucidate the properties of Π_n and to understand the structure of its parameter space by exploring how the stable and unstable fixed points of Π_n are created. To that effect it will be useful to include not only positive, but also negative values of $d^\star$ to the domain of Π_n. But it is important to add that values $d^\star < 0$ are biologically impossible as the depression variable models a finite pool of neurotransmitters, and therefore must be positive. Because Π_n maps first from $d^\star$ to Δt, and then back to $d^\star$, we will also consider negative values of Δt, interpreting them as $n - n$ solutions with partially overlapping bursts. As will become evident,

$\Delta t < 0$ is only a formal violation of the biological realism of the map Π_n, as numerically stable $n - n$ solutions of the full system of ODEs only exist for $\Delta t > 0$.

We start the construction of Π_n by first considering the free phase and building the map F_n. At each spike time t_k, variable d depresses with the reset $d(t_k) \leftarrow \lambda d(t_k^-)$ (eq. (8)). For the duration of the subsequent ISI, the recovery of d is described by the solution to eq. (6):

$$d(t) = 1 - (1 - \lambda d_k)e^{-t/\tau_d} \ , \tag{15}$$

where the variable $d_k = d(t_k^-)$ is the level of depression at spike time t_k. By substituting $t = T$ we can build a linear map that models the depression of d from spike time t_k to the subsequent spike time t_{k+1} during the free phase:

$$d_{k+1} = \lambda \rho d_k + (1 - \rho), \tag{16}$$

where to keep the notation simple we let $\rho = \exp(-T/\tau_d)$. Since $0 < \lambda, \rho < 1$, the map (16) is increasing and contracting, with a fixed point at

$$d_s = \frac{1 - \rho}{1 - \lambda \rho}, \tag{17}$$

where $0 < d_s < 1$. The value d_s is the maximum depression value that can be observed in the suppressed solution where the active cell fires at its uncoupled period T (see fig. 3E). Using the release condition in eq. (9) allows

us to derive the value of the the minimum coupling strength that will produce the full suppressed solution, denoted as $\bar{g}_s$. Solving eq. (5) for $s(t)$ with $t = T$ and setting the initial value $s(0) = d_s$ gives

$$\bar{g}_s d_s e^{-T/\tau_s} = g^\star. \tag{18}$$

By further substituting the definition of d_s in (17) and rearranging, we can write $\bar{g}_s$ as a function of the depression strength λ:

$$\bar{g}_s(\lambda) = g^\star e^{T/\tau_s} \frac{1 - \lambda\rho}{1 - \rho}. \tag{19}$$

Note that the above dependence of $\bar{g}_s$ on λ is linear and monotonically decreasing. Increasing λ reduces the strength of the depression of the free cell. This in turn allows the free cell to fully suppress the quiet cell at smaller values of $\bar{g}$.

Solving (16) gives us the linear map $\delta_n : d^\star \mapsto d_n$, that for some initial $d^\star$ computes the depression at the nth spike time, $d_n = d(t_n^-)$:

$$\delta_n(d^\star) = (\lambda\rho)^{n-1} d^\star + (1 - \rho) \sum_{i=0}^{n-2} (\lambda\rho)^i. \tag{20}$$

Since $\lambda < 1$, function δ_n is a linearly increasing function of $d^\star$ with a fixed point at d_s for all n. Having identified d after n spikes, we can now use the release condition $\bar{g}s = g^\star$ (eq. (9)) to find Δt. At the last spike of the free phase at time $t_n = (n - 1)T$ the synapse variable s is reset according to

eq. (7):

$$s(t_n) \leftarrow \delta_n(d^\star). \tag{21}$$

After the last spike s decays exponentially according to the solution of eq. (5), where setting the initial condition $s(0) = \delta_n(d^\star)$ yields:

$$s(\Delta t) = \delta_n(d^\star) e^{-\Delta t/\tau_s}. \tag{22}$$

Substituting $s(\Delta t)$ into s of the release condition (eq. (9)) gives then

$$\bar{g}\delta_n(d^\star) e^{-\Delta t/\tau_s} = g^\star. \tag{23}$$

Our assumption of the release condition guarantees that the quiet cell 2 spikes and becomes free when $\bar{g}s - g^\star$ crosses zero. Solving eq. (23) for Δt allows us to compute the inter-spike-interval as a function of $d^\star$, which defines our map F_n:

$$F_n(d^\star) := \tau_s \ln\left(\frac{\bar{g}}{g^\star}\delta_n(d^\star)\right) = \Delta t. \tag{24}$$

Figure 9A shows F_n for various n, which is a strict monotonically increasing function of $d^\star$ as well as $\bar{g}$. Larger values of $d^\star$ and $\bar{g}$, respectively, cause stronger inhibition of the quiet cell, and therefore prolong its release time and the associated Δt. Map F_n is defined on $d^\star > d_a$, where d_a is a vertical asymptote found by solving $\delta_n(d^\star) = 0$ in eq. (20) for $d^\star$, which yields

$$d_a(n) = -\frac{(1-\rho)\sum_{i=0}^{n-2}(\lambda\rho)^i}{(\lambda\rho)^{n-1}} \leq 0\ . \tag{25}$$

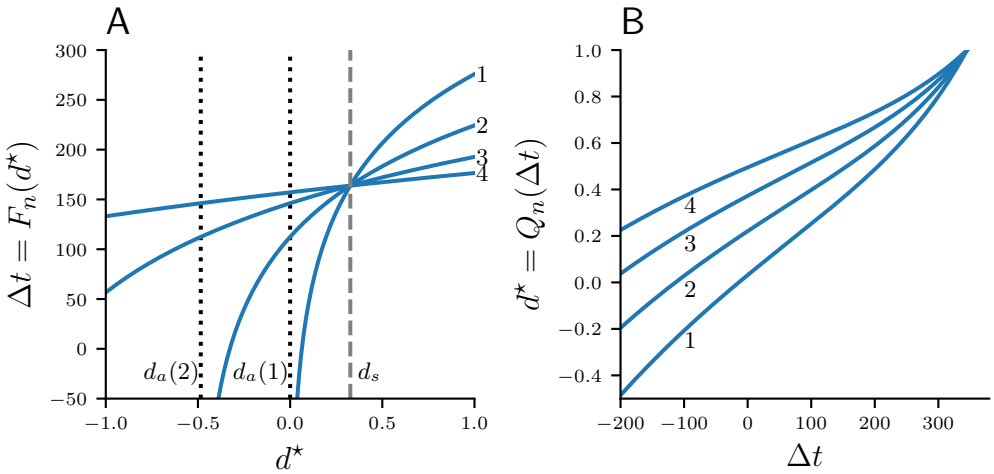

Figure 9: Maps F_n (**A**) and Q_n (**B**) for $\bar{g} = 0.6$ mS/cm^2 and $n = 1, 2, 3, 4$. Curves F_n intersect at d_s which is indicated by a dashed vertical line.

We now turn to the construction of map Q_n, which describes the recovery of the depression variable during the quiet phase. As we have identified earlier, the recovery in the quiet phase of a $n - n$ solution is of duration $2\Delta t + (n-1)T$. Substituting that into the solution for $d(t)$ (eq. (15)) with the initial condition $d(0) = \delta_n(d^\star)$ yields the map Q_n:

$$Q_n(\Delta t) := 1 - (1 - \lambda\delta_n(d^\star))e^{-(2\Delta t + (n-1)T)/\tau_d}. \tag{26}$$

Given Δt, we can find $\delta_n(d^\star)$ by rearranging the release condition in eq. (23):

$$\delta_n(d^\star) = \frac{g^\star}{\bar{g}} e^{\Delta t/\tau_s}. \tag{27}$$

Map Q_n is shown in fig. 9B for various values n. Note that Q_n is monotoni-

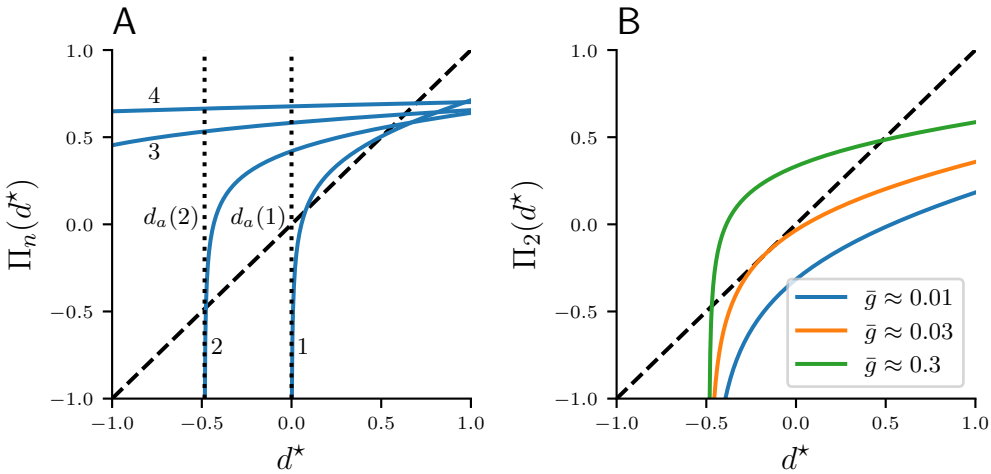

Figure 10: Map $\Pi_n : d^\star$. **A**: Π_n for $n = 1, 2, 3, 4$ at $\bar{g} = 0.6$ mS/cm^2. **B**: Π_2 with $n = 2$ for varying $\bar{g} \approx 0.01, 0.034, 0.3$ mS/cm^2. The identity function is illustrated by a diagonal line.

cally increasing as larger values Δt imply a longer recovery time, and hence Q_n grows without bound. All curves Q_n intersect at some $\Delta t = \tau_s \ln[\bar{g}/(g^\star \lambda)]$ where

$$Q_n \left[\tau_s \ln \left(\frac{\bar{g}}{g^\star \lambda} \right) \right] = 1. \tag{28}$$

As we will show in the next section, all fixed points of the full map Π_n occur for $d^\star < 1$. We will therefore restrict the domain of Q_n to $(-\infty, \ln[\bar{g}/(g^\star \lambda)]\tau_s)$ and the codomain to $(-\infty, 1)$. Additionally, while values $\Delta t > T$ will be helpful in exploring the geometry of Π_n, recall from fig. 8 that in the flow system all $n - n$ solutions bifurcate into $(n+1) - (n+1)$ solutions exactly when $\Delta t = T$, and we will address this concern in the last part of our map analysis.

Having found F_n and Q_n, we can now construct the full map $\Pi_n(d^\star) =$

$Q_n\big(F_n(d^\star)\big)$:

$$\Pi_n(d^\star) = 1 - \frac{\rho^{n-1} g^{\star\tau}}{\bar{g}^\tau} \delta_n^{-\tau}(d^\star)\big(1 - \lambda\delta_n(d^\star)\big), \tag{29}$$

where we substituted $\tau = 2\tau_s/\tau_d$. Since d is the slowest variable of the system and $\tau_d \gg \tau_s$, we will also assume $\tau < 1$. Figure 10A depicts Π_n for various n. Intersections of Π_n with the diagonal are fixed points of the map. Figure 10B shows Π_2 with $n = 2$. Varying the synaptic strength $\bar{g}$ moves the curves Π_n up and down the $(d^\star, \Pi_n)$-plane. For $\bar{g} < 0.03$ mS/cm^2 map Π_2 has no fixed points. As $\bar{g}$ is increased to $\bar{g} \approx 0.03$ mS/cm^2, curve Π_2 coalesces with the diagonal tangentially. When $\bar{g} > 0.03$ mS/cm^2, a pair of fixed points emerge, one stable and one unstable fixed point, indicating the occurrence of a fold bifurcation of maps.

From eq. (29) it is evident that Π_n is monotonically increasing with respect to $\bar{g}$ and also $d^\star$:

$$\frac{\mathrm{d}\Pi_n}{\mathrm{d}\bar{g}} > 0, \tag{30}$$

$$\frac{\mathrm{d}\Pi_n}{\mathrm{d}d^\star} > 0, \tag{31}$$

and in the following sections we will heavily rely on this monotonicity property of Π_n. Just as F_n, curves Π_n spawn at the asymptote d_a (eq. (25)), and because

$$\lim_{\bar{g}\to\infty} \Pi_n = 1 \text{ for all } n, \tag{32}$$

fixed points of Π_n lie in $(d_a, 1)$.

3.4. Existence and stability of fixed points of Π_n

We introduce the fixed point notation $d_f^\star$ with $\Pi_n(d_f^\star) = d_f^\star$. The existence of fixed points $d_f^\star$ for $\bar{g}$ sufficiently large can be shown from the strict monotonicity of Π_n with respect to $\bar{g}$ and $d^\star$ (eqs. (30) and (31)), as well as the fact that the slope of Π_n is monotonically decreasing,

$$\left(\frac{\mathrm{d}}{\mathrm{d}d^\star}\right)^2 \Pi_n < 0. \tag{33}$$

In the limit $d^\star \to d_a$ the value of Π_n decreases without bound for any $\bar{g} > 0$. For $d^\star > d_a$ the value of Π_n depends on $\bar{g}$. In the limit $\bar{g} \to 0$, Π_n also decreases without bound, but as $\bar{g} \to \infty$ values of Π_n approach 1. It follows from eq. (30) and the intermediate value theorem that for some $\bar{g}$ large enough Π_n intersects the diagonal. Moreover, because Π_n and its slope are monotonic with respect to $d^\star$, there exists some critical fixed point $(d_b^\star, \bar{g}_b)$ where Π_n aligns with the diagonal tangentially with

$$\Pi_n(d_b^\star; \bar{g}_b) = d_b^\star, \tag{34}$$

$$\frac{\mathrm{d}}{\mathrm{d}d^\star}\Pi_n(d_b^\star; \bar{g}_b) = 1. \tag{35}$$

Equations (30) and (33) constitute the non-degeneracy conditions for a codimension-1 fold bifurcation of maps, indicating that in a neighbourhood of $(d_b^\star, \bar{g}_b)$ map

Π_n has the topological normal form described by the graph of

$$x \mapsto \beta + x - x^2, \tag{36}$$

with a stable and unstable fixed point $x = \pm\sqrt{\beta}$, and slopes $\mathrm{d}x/\mathrm{d}\beta = \mp(2\sqrt{\beta})^{-1}$, respectively.

3.5. Fold bifurcations of Π_n

Fixed points of Π_n satisfy the fixed point equation $\Phi_n(d^\star; \bar{g}) = 0$, where

$$\Phi_n(d^\star, \bar{g}) := \Pi_n(d^\star, \bar{g}) - d^\star. \tag{37}$$

As we have already shown, for $\bar{g} > \bar{g}_b(n)$ solutions to eq. (37) exist in pairs of stable and unstable fixed points. Solving eq. (37) explicitly for $d^\star$ it not trivial, but solving for $\bar{g}$ is straightforward and given by $\bar{g} = G_n(d^\star)$, where

$$G_n(d^\star) := g^\star \left(\frac{\rho^{n-1}\delta_n^{-\tau}(d^\star)(1 - \lambda\delta_n(d^\star))}{1 - d^\star} \right)^{1/\tau}. \tag{38}$$

Plotting $d^\star$ against $\bar{g}$ gives the fixed point curves, which are shown in fig. 11A. Note the typical quadratic shape of a fold bifurcation of maps. It is also evident that the fold bifurcations occur for increasingly smaller $\bar{g}$ as n is increased. Moreover, we can observe that unstable fixed points have negative values of $d^\star$ for $n > 1$.

Equation (38) also allows us to find the critical fixed point connected with the fold bifurcation, namely $\big(d_b^\star(n), \bar{g}_b(n)\big)$, which is the global minimum of

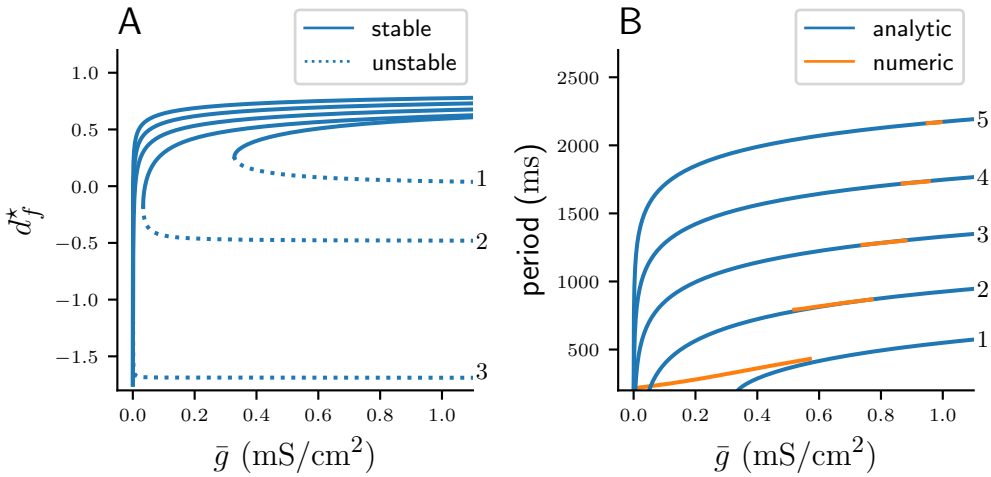

Figure 11: **A**: Fold bifurcation diagrams of stable (continuous curves) and unstable (dotted curves) fixed points of Π_n for varying n. **B**: Cycle periods computed from stable fixed points (blue), and the corresponding solution period from numerical integration of the system of ODEs (orange).

$G_n(d_f^\star)$:

$$d_b^\star(n) = \operatorname{argmin} G_n(d_f^\star), \tag{39}$$

$$\bar{g}_b(n) = \min G_n(d_f^\star). \tag{40}$$

Function G_n is strictly monotonic on the respective intervals of $d_f^\star$ that correspond to the stable and unstable fixed points, that is

$$\frac{\mathrm{d}G_n}{\mathrm{d}d_f^\star} < 0, \text{ for } d_f^\star > d_b^\star(n) \text{ stable}, \tag{41}$$

$$\frac{\mathrm{d}G_n}{\mathrm{d}d_f^\star} > 0, \text{ for } d_f^\star < d_b^\star(n) \text{ unstable}, \tag{42}$$

which allows us to express the stable and unstable fixed points as the inverse of G_n on their respective intervals of $d_f^\star$. Because we are primarily interested in the stable fixed points, we define the stable fixed point function $d_f^\star = \phi_n(\bar{g})$ as

$$\phi_n(\bar{g}) := G_n^{-1}(d_f^\star) \text{ for } d_f^\star > d_b^\star(n). \tag{43}$$

Function $\phi_n(\bar{g})$ is also monotonic, and is therefore straightforward to compute numerically via root-finding. Here we use the Python package Pynverse (Gonzalez, 2021) for that purpose.

Having found the stable fixed points $d_f^\star$ as a function of the coupling strength $\bar{g}$, we can now compute the associated cycle period. Recall that the period is given by eq. (10), which we can be written as a function of $\bar{g}$:

$$P_n(\bar{g}) = 2(n-1)T + 2F_n\big(\underbrace{\phi_n(\bar{g})}_{d_f^\star}, \bar{g}\big), \tag{44}$$

where map F_n (eq. (24)) calculates the inter-burst-interval Δt given a stable fixed point $d_f^\star = \phi_n(\bar{g})$. We plot the predicted period $P_n(\bar{g})$ versus the cycle period that was computed from numerically integrating the full system of ODEs in fig. 11B. For $n > 1$ our map Π_n accurately predicts the period. When laying out our assumptions in section 3.2, we have already predicted an inaccuracy for $n = 1$ (see fig. 6), since here $\bar{g}$ is not sufficiently strong to guarantee the validity of our release condition (eq. (9)).

It is evident from fig. 11A that ϕ_n is strictly increasing with $\bar{g}$. This prop-

erty follows directly from the normal form of the fold bifurcation (eq. (36)), but can also be shown using implicit differentiation and the fixed point equation $\Phi_n(\phi_n(\bar{g}), \bar{g}) = 0$ in eq. (37). For $d_f^\star = \phi_n(\bar{g}) > d_b(n)$ we get:

$$\frac{\mathrm{d}\phi_n}{\mathrm{d}\bar{g}} = -\frac{\partial\Phi_n/\partial\bar{g}}{\partial\Phi_n/\partial d^\star} = \frac{\partial\Pi_n/\partial\bar{g}}{1 - \partial\Pi_n/\partial d^\star} > 0. \tag{45}$$

The inequality follows from $\partial\Pi_n/\partial\bar{g} > 0$ and the fact that $\partial\Pi_n/\partial d^\star < 1$ for $d^\star > d_b(n)$. Equation (45) allows us to explain why the period P_n increases with $\bar{g}$, as seen in fig. 11B. Differentiating P_n gives:

$$\frac{\mathrm{d}P_n}{\mathrm{d}\bar{g}} = 2\boldsymbol{\nabla} F_n(d_f^\star, \bar{g}) \cdot \begin{bmatrix} \partial\phi_n/\partial\bar{g} \\ 1 \end{bmatrix} > 0, \tag{46}$$

where the partial derivatives of $F_n(d_f^\star, \bar{g})$ are:

$$\frac{\partial F_n}{\partial d_f^\star} = \tau_s \frac{(\lambda\rho)^{n-1}}{\delta_n(d_f^\star)} > 0, \tag{47}$$

$$\frac{\partial F_n}{\partial \bar{g}} = \frac{\tau_s}{\bar{g}} > 0. \tag{48}$$

Equations (45) and (46) have an intuitive biological interpretation: Increasing the coupling strength between the neurons leads to overall stronger inhibition of the quiet cell, which delays its release and leads to a longer cycle period. The latter allows more time for the synapse to depress in the free phase and recover in the quiet phase, resulting in overall larger values of $d_f^\star$, that is weaker depression at the burst onset.

While fixed points of our Poincaré map predict the cycle period of the flow system excellently, its construction relies on the strong assumption that the free phase contains exactly n spikes. As is evident from fig. 11B this assumption is clearly violated in the flow system, as stable $n-n$ bursts exists only on certain parameter intervals of $\bar{g}$. In the last sub-section we will analyse the mechanisms that guide how the stable $n-n$ are created and destroyed, and use our previous analysis to derive the corresponding parameter intervals of $\bar{g}$ where such solutions exist.

3.6. Period increment bifurcations with co-existent attractors

Let $\bar{g}_+(n)$ and $\bar{g}_-(n)$ denote the left and right parameter borders on $\bar{g}$ where stable $n-n$ solutions exist. That is, as $\bar{g}$ is increased stable $n-n$ solutions are created at $\bar{g}_+(n)$ and destroyed at $\bar{g}_-(n)$. When $\bar{g}$ is reduced beyond $\bar{g}_+(n)$, $n-n$ solutions bifurcate into $(n-1)-(n-1)$ solutions, while when $\bar{g}$ is increased beyond $\bar{g}_-(n)$, $n-n$ solutions bifurcate into $(n+1)-(n+1)$ solutions. Let us briefly recap our observations regarding $\bar{g}_+(n)$ and $\bar{g}_-(n)$ from the numerical bifurcation diagram in fig. 11B. For $n > 1$ there are the following relations:

$$\bar{g}_+(n) < \bar{g}_-(n), \tag{49}$$

$$\bar{g}_+(n) < \bar{g}_+(n+1) \text{ and } \bar{g}_-(n) < \bar{g}_-(n+1), \tag{50}$$

$$\bar{g}_+(n+1) < \bar{g}_-(n), \tag{51}$$

$$\bar{g}_-(n+1) - \bar{g}_+(n+1) < \bar{g}_-(n) - \bar{g}_-(n). \tag{52}$$

Equations (49) and (50) are self-explanatory. Equation (51) formally describes occurrence of co-existence between stable $n-n$ and $(n+1)-(n+1)$ solutions. Equation (52) implies that the parameter interval on $\bar{g}$ of $n-n$ solutions decreases with n, in other words, bursts with more spikes occur on increasingly smaller intervals of the coupling strength. All of the above relations are reminiscent of the period-adding bifurcations with co-existent attractors, first described for piecewise-linear scalar maps with a single discontinuity by Avrutin and colleagues (e.g. see Gardini et al., 2012; Tramontana et al., 2012; Avrutin et al., 2011, 2012).

Let us now find algebraic equations that will allow us to calculate the critical parameters $\bar{g}_+(n)$ and $\bar{g}_-(n)$ associated with the period-increment bifurcations. Recall that the period P_n derived from the fixed points of Π_n is an increasing function of $\bar{g}$:

$$\frac{\mathrm{d}P_n}{\mathrm{d}\bar{g}} = 2\frac{\mathrm{d}F_n(\phi_n(\bar{g}), \bar{g})}{\mathrm{d}\bar{g}} > 0, \tag{53}$$

that is, as the coupling strength increases, it takes longer for the total synaptic conductance to fall below the value of the release conductance, which delays the release of the quiet cell, and Δt becomes larger. Once $\Delta t = T$, the free cell can produce another spike and the solution bifurcates into a $(n+1)-(n+1)$ solution. Note, however, that at $\bar{g}_+(n)$ the bifurcation into a $(n-1)-(n-1)$ does not occur when $\Delta t = 0$. Here the mechanism is different: A sufficient reduction of $\bar{g}$ causes the total synaptic conductance

to drop below the release conductance in the *previous* ISI, which allows the quiet cell to be released one spike earlier.

Using the above reasoning we can now formulate the conditions for both bifurcations at $\bar{g}_+(n)$ and $\bar{g}_-(n)$. As in the previous sections, we will only restrict ourselves to the analysis of the stable fixed points given implicitly by $d_f^\star = \phi_n(\bar{g})$ (eq. (43)). At the right bifurcation border $\bar{g}_-(n)$ we have $\Delta t = T$, and after substituting our F_n-map (eq. (24)) this translates into

$$F_n(\phi_n(\bar{g}), \bar{g}) = T, \tag{54}$$

which lets us define a function

$$R_n(\bar{g}) := F_n(\phi_n(\bar{g}), \bar{g}) - T, \tag{55}$$

whose root is the desired right bifurcation border $\bar{g}_-(n)$. In case of the left bifurcation border at $\bar{g}_+(n)$ the release condition is satisfied just before the free cell has produced its nth spike, and after the depression variable has been reset $n-1$ times, which gives the condition

$$\bar{g}\delta_{n-1}\big(\phi_n(\bar{g})\big)e^{-T/\tau_s} = g^\star, \tag{56}$$

and can be rewritten as a function

$$L_n(\bar{g}) := \bar{g}\delta_{n-1}\big(\phi_n(\bar{g})\big)e^{-T/\tau_s} - g^\star, \tag{57}$$

whose root is $\bar{g}_+(n)$. Both R_n and L_n are increasing with respect to $\bar{g}$, which makes finding their roots numerically straightforward.

Figure fig. 12 shows the period $P_n(\bar{g})$ as predicted by the fixed points of Π_n (eq. (44)) plotted on their respective intervals $\bar{g} \in [\bar{g}_+(n), \bar{g}_-(n)]$ (blue), as well as the cycle period acquired from numerical integration of the full system of ODEs (orange). Note that the width of $n-n$ branches decreases with n, which confirms the inequality in eq. (52). That is, bursts with more spikes occur on increasingly smaller intervals of $\bar{g}$, which can be interpreted as a lost of robustness with respect to the coupling strength of long-cyclic solutions. We also note the occurrence of bi-stability between pairs of $n-n$ and $(n+1)-(n+1)$ branches, which also confirms our initial observation in eq. (51).

As previously observed in fig. 11B our maps prediction of the cycle period is accurate for $n > 1$. Recall that our reduction assumptions required a sufficiently large coupling strength, which we numerically estimated to be $\bar{g} \approx 0.592\text{mS/cm}^2$ in fig. 6. The mismatch in period for $1-1$ solutions, but also the mismatch in the left bifurcation border $\bar{g}_-(n=2)$ of the $2-2$ solution can be attributed to the violation of that assumption. However, even for branches of large $n-n$ solutions there is a mismatch between the bifurcation borders. Presumably our assumptions on the time scales of w and s dynamics do not hold here, and can only be captured by more complex approximations. Nevertheless, our map allows approximate extrapolation of the cycle period and the respective bifurcation borders where numerical

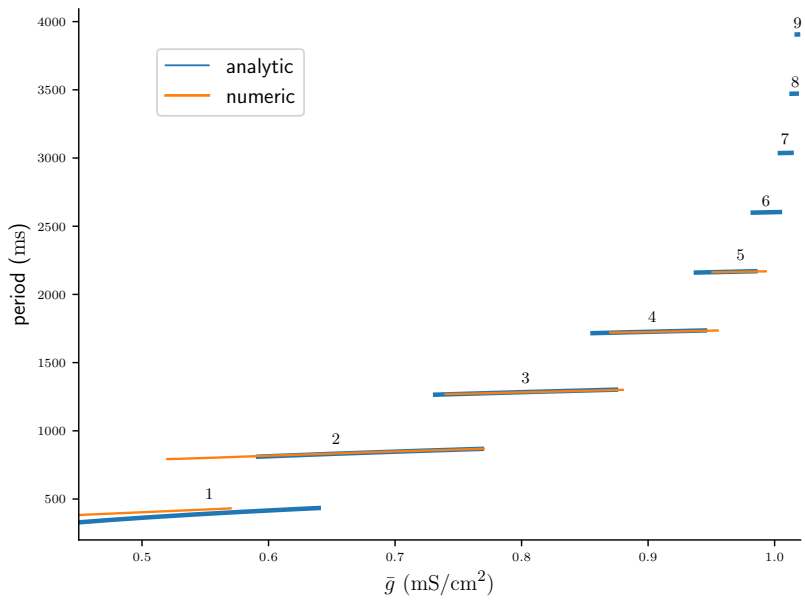

Figure 12: Bifurcation diagrams of stable $n - n$ solutions computed analytically from fixed points of Π_n and plotted on the respective intervals of $\bar{g} \in \left[\bar{g}_+(n), \bar{g}_-(n)\right]$ (blue), and computed from numerical integrations of the ODEs (orange).

integration of the ODEs would require a very small time step.

4. Discussion

Synaptic depression of inhibition is believed to play an important role in the generation of rhythmic activity involved in many motor rhythms such as in leech swimming (Mangan et al., 1994) and leech heart beat (Calabrese et al., 1995), and in the lobster pyloric system (Manor et al., 1997; Rabbah & Nadim, 2007). In half-centre CPGs synaptic depression can act as a burst termination mechanism, enabling the alternation of bursting between the two sides of the CPG (Brown, 1911). The struggling escape behaviour in *Xenopus*

tadpoles is one such motor rhythm that is thought to be driven by synaptic depression of reciprocal inhibition between the two sides of the tadpole spinal cord (Li et al., 2007). Mathematical modelling can shed light on the underlying mechanisms that enable the generation of such anti-phase bursts in struggling, and help identify the components that control this rhythm allowing it to switch between different patterns.

To study the mechanisms of burst generation in tadpole struggling we have analysed a neuronal model network that consists of a pair of inhibitory neurons that undergo a frequency dependent synaptic depression. When the strength of synaptic inhibition between the neurons is varied, such a simple network can display a range of different struggling-like $n-n$ burst patterns. Using the timescale disparity between neuronal and synaptic dynamics, we have reduced the network model of eight ODEs to a scalar first return map Π_n of the slow depression variable d. This map Π_n is a composition of two maps, F_n and Q_n, that model the evolution of the depression during the free and quiet phases of $n-n$ solutions respectively. Both F_n and Q_n maps are constructed by using the dynamics of single uncoupled neurons. Fixed points of Π_n are created in pairs through a fold bifurcation of maps, where the stable fixed point correspond to stable $n-n$ burst solutions of the full two-cell system of ODEs. The results from our one-dimensional map match excellently with numerical simulation of the full struggling network. In line with Brown's 1911 rhythmogenesis hypothesis, our results support the idea that synaptic depression in tadpoles may act as a burst termination

mechanism which produces the anti-phase patterns found in struggling (Li et al., 2007).

We have studied $n - n$ solutions assuming that the synaptic coupling $\bar{g}$ between the two cells is symmetrical. However, Bose & Booth (2011) have shown that asymmetrical coupling $(\bar{g}_1, \bar{g}_2)$ can result in network solutions of type $m - n$, where one cell fires m spikes, while the other n spikes. It is conceivable that our map construction can be extended to also capture such $m - n$ solutions. Remember, in the case of symmetrical coupling with $n - n$ solutions, the timecourse of the depression variables d_1 and d_2 were in anti-phase, and it was therefore sufficient to track only one of the two variables. To capture the full network dynamics in case of asymmetrical coupling one would also have to account for burst patterns of type $m - n$, where the solutions of the depression variables d_1 and d_2 are not simply time-shifted versions of each other. To do that, one could track the state of both variables by constructing a two-dimensional Poincaré map $\Pi(d_1, d_2)$. While geometrical interpretation of two-dimensional maps remains challenging, there exist a number of recent studies which have employed novel geometrical analysis methods to understand the dynamics of two-dimensional maps of small neuronal networks (Akcay et al., 2014, 2018; Liao et al., 2020). Generally speaking, our map construction approach is applicable to any small network, even with more than two neurons. As long as the network dynamics occur on separable timescales the main challenges to the map construction lie in identifying the slowest variables, and finding an appropriate, simplified de-

scription of their respective timecourses. In theory, the reduction approach can be also applied to neuronal systems with more than two timescales (e.g. see Kuehn, 2015).

Struggling in tadpoles is initiated by an increase in cIN firing frequency, which has been hypothesised to lead to stronger synaptic depression of commissural inhibition and result in the iconic anti-phase bursting (Li et al., 2007). It would therefore be interesting to study how varying the cell intrinsic firing period T could affect the network rhythm. While we have laid out the framework to perform such an investigation, due to the choice of neural model we have avoided varying T. Recall that T is a derived parameter in the Morris & Lecar (1981) model, and can therefore not be varied in isolation of other model parameters. This makes verifying any analytical results from our map analysis via numerical integration of the ODEs difficult. A more abstract model such as the quadratic integrate-and-fire model (Izhikevich, 2004) allows varying T independently of other model parameters, and could be more fitting in this scenario.

Our simulations of the network showed that $n - n$ solutions lose robustness as their period is increased. That is, solutions with a larger cycle period occur on increasingly smaller intervals of the coupling strength. We were able to replicate this finding by numerically finding the respective left and right borders of stable $n-n$ branches of fixed points of Π_n, and showing that the distance between these borders shrinks with n. We have also noted the resemblance of our bifurcation diagram to one where such $n - n$ branches

are created via a period-increment bifurcation with co-existent attractors of scalar linear maps with a discontinuity (Avrutin et al., 2012, 2011). It is worthwhile noting that the bifurcations of piecewise linear maps studied by Avrutin et al. and colleagues result from a "reinjection" mechanism, first described by Perez (1985). Here the orbit of a map performs multiple iterations on one side of the discontinuity, before jumping to the other side and being *reinjected* back into the initial side of the discontinuity. The stark difference of such a map to our map is that reinjection allows a *single* scalar map to produce periodic solutions of varying periods. In contrast, we rely on n different maps Π_n to describe the dynamics burst dynamics without explicitly capturing the period increment bifurcations. It is therefore conceivable that despite the complexity and non-linearity of the dynamics of our two-cell network, a single piecewise-linear map might be already sufficient to capture the mechanisms that shape the parameter space of the full system. In their discussion, Bose & Booth (2011) briefly outline ideas about how such a linear map could be constructed.

In addition to stable $n-n$ solutions, the numerical continuation by Bose & Booth (2011) also revealed branches of unstable $n-n$ solutions. While we have identified fold bifurcations of our burst map, we have not found corresponding bifurcations of the flow ODE system, and have generally ignored the significance of unstable map fixed points. However, our results are reminiscent of a saddle homoclinic orbit bifurcation, where a stable periodic orbit collides with a saddle equilibrium, and its period becomes infinite. A

number of theoretical studies have investigated such a *homoclinic tangency to a periodic orbit* in higher-dimensional systems (e.g. Gavrilov & Shilnikov, 1972; Gaspard & Wang, 1987), and a next step would be to provide a rigorous explanation of not only the map dynamics, but also of the flow dynamics of the ODE system.

We have shown that when the strength of the maximum synaptic conductance is varied, synaptic depression of inhibition can enable our two-cell network to produce burst solutions of different periods. This result is in line with the idea that one role of synaptic depression in the nervous system may be to allow a finite size neuronal network to participate in different tasks by producing a large number of rhythms (Bose & Booth, 2011; Jalil et al., 2004; Li et al., 2007). To change from one rhythm to another would only require a reconfiguration of the network through changes in synaptic coupling strength, which can occur through the process of learning. Thus short-term synaptic depression of inhibition may provide means for a network to adapt to environmental challenges without changing its topology, that is without the introduction or removal of neurons.

5. Acknowledgements

Funding: This work was supported by the Wellcome Trust Doctoral Training Programme in Neural Dynamics, Grant no. 099699/Z/12/Z.

We thank Alan Champneys for sharing his insights on non-continuous maps during the course of this research. We are also grateful to Alan Roberts

and Stephen R. Soffe for their comments on earlier versions of the manuscript.

Appendix A. Model equations and parameters

The asymptotic functions m_∞ and w_∞ for the calcium and potassium conductances, respectively, are given by

$$m_\infty(v_i) = \frac{1}{2}\left(1 + \tanh\left((v_i - v_A)/v_B\right)\right), \tag{A.1}$$

$$w_\infty(v_i) = \frac{1}{2}\left(1 + \tanh\left((v_i - v_C)/v_D\right)\right). \tag{A.2}$$

Model parameters were adapted from Bose & Booth (2011) and are given in table A.1:

Appendix B. Computing bifurcation diagram numerically

The bifurcation diagram of stable $n-n$ solutions of the two-cell network in fig. 4 is obtained numerically as follows: We initialise the coupling strength at parameter values associated with one type of $n-n$ solution, that is we choose the values $\bar{g} = 0.4, 0.7, 0.8, 0.9, 0.98$ for the $1-1$, $2-2$, $3-3$, $4-4$, and $5-5$ solutions respectively. For each $\bar{g}$ the system is then numerically integrated sufficiently long for any transients to fully subside. We then identify one period of the solution by finding the first return of the depression variable d_1. That is, we choose some value d_k at a spike time t_k, and by iterating from spike to spike find some subsequent value d_{k+1} at spike time such that $|d_{k+1} - d_k| < \epsilon$. If a periodic solution of type $n-n$ is found in such way, $\bar{g}$ is step-

Table A.1: Default parameters for coupled Morris-Lecar model.

Parameter	value
g_{L}	0.15 mS/cm^2
g_{Ca}	0.3 mS/cm^2
g_{K}	0.6 mS/cm^2
v_{L}	-50 mV
v_{Ca}	100 mV
v_{K}	-70 mV
v_A	1 mV
v_B	14.5 mV
v_C	4 mV
v_D	15 mV
I	6 μA/cm^2
τ_w	100 ms
τ_d	1000 ms
τ_s	100 ms
v_θ	0 mV
v_s	-80 mV
λ	0.5
T	217 ms
$g^\star$	0.03804 mS/cm^2

wise increased/decreased, and the above algorithm is repeated. Otherwise, the set of all previously found solutions and the corresponding values $\bar{g}$ are returned.

Note that applying conventional methods of numerical continuation is not straightforward for our model, as the discontinuous resets in eq. (7) and (8) make the root finding challenging (e.g. see Kuznetsov, 2004, for continuation methods).

References

Akcay, Z., Bose, A., & Nadim, F. (2014). Effects of synaptic plasticity on phase and period locking in a network of two oscillatory neurons. *The Journal of Mathematical Neuroscience*, *4*, 8. doi:10.1186/2190-8567-4-8.

Akcay, Z., Huang, X., Nadim, F., & Bose, A. (2018). Phase-locking and bistability in neuronal networks with synaptic depression. *Physica D: Nonlinear Phenomena*, *364*, 8 – 21. doi:10.1016/j.physd.2017.09.007.

Avrutin, V., Granados, A., & Schanz, M. (2011). Sufficient conditions for a period incrementing big bang bifurcation in one-dimensional maps. *Nonlinearity*, *24*, 2575–2598. URL: https://doi.org/10.1088/0951-7715/24/9/012. doi:10.1088/0951-7715/24/9/012.

Avrutin, V., Schanz, M., & Schenke, B. (2012). Breaking the continuity of a piecewise linear map. *ESAIM: Proceedings*, *36*, 73–105. URL: https://doi.org/10.1051/proc/201236008. doi:10.1051/proc/201236008.

Bose, A., & Booth, V. (2011). Co-existent activity patterns in inhibitory neuronal networks with short-term synaptic depression. *Journal of Theoretical Biology*, *272*, 42–54. doi:10.1016/j.jtbi.2010.12.001.

Bose, A., Manor, Y., & Nadim, F. (2001). Bistable oscillations arising from synaptic depression. *SIAM Journal on Applied Mathematics*, *62*, 706–727. doi:10.1137/S0036139900378050.

Brown, T. G. (1911). The intrinsic factors in the act of progression in the mammal. *Proceedings of the Royal Society of London. Series B*, *84*, 308–319.

Calabrese, R. L., Nadim, F., & Olsen, Ø. H. (1995). Heartbeat control in the medicinal leech: A model system for understanding the origin, coordination, and modulation of rhythmic motor patterns. *Journal of neurobiology*, *27*, 390–402. doi:10.1002/neu.480270311.

Clarke, J. D., Hayes, B. P., Hunt, S. P., & Roberts, A. (1984). Sensory physiology, anatomy and immunohistochemistry of Rohon-Beard neurones in embryos of *Xenopus laevis*. *The Journal of Physiology*, *348*, 511–525. doi:10.1113/jphysiol.1984.sp015122.

Donovan, M., Wenner, P., Chub, N., Tabak, J., & Rinzel, J. (1998). Mechanisms of spontaneous activity in the developing spinal cord and their relevance to locomotion. *Annals of the New York Academy of Sciences*, *860*, 130–141.

Ermentrout, B. (2002). *Simulating, analyzing, and animating dynamical systems: a guide to xppaut for researchers and students*. SIAM.

Ermentrout, G. B., & Terman, D. H. (2010). *Mathematical foundations of neuroscience* volume 35 of *Interdisciplinary Applied Mathematics*. Springer New York. doi:10.1007/978-0-387-87708-2.

Friesen, W. O. (1994). Reciprocal inhibition: a mechanism underlying oscillatory animal movements. *Neuroscience & Biobehavioral Reviews*, *18*, 547–553. doi:10.1016/0149-7634(94)90010-8.

Gardini, L., Avrutin, V., Schanz, M., Granados, A., & Sushko, I. (2012). Organizing centers in parameter space of discontinuous 1d maps. the case of increasing/decreasing branches. *ESAIM: Proceedings*, *36*, 106–120. URL: https://doi.org/10.1051/proc/201236009. doi:10.1051/proc/201236009.

Gaspard, P., & Wang, X. J. (1987). Homoclinic orbits and mixed-mode oscillations in far-from-equilibrium systems. *Journal of Statistical Physics*, *48*, 151–199. doi:10.1007/BF01010405.

Gavrilov, N. K., & Shilnikov, L. P. (1972). On three-dimensional dynamical systems close to systems with a structurally unstable homoclinic curve. I. *Mathematics of the USSR-Sbornik*, *17*, 467. doi:10.1070/SM1972v017n04ABEH001597.

Gonzalez, A. S. (2021). pynverse. https://github.com/alvarosg/pynverse.

Izhikevich, E. M. (2004). Which model to use for cortical spiking neurons? *ieee transactions on neural networks*, *15*, 1063–1070. doi:10.1109/TNN.2004.832719.

Jalil, S., Grigull, J., & Skinner, F. K. (2004). Novel bursting patterns emerging from model inhibitory networks with synaptic depression. *Jour-*

nal of Computational Neuroscience, *17*, 31–45. doi:10.1023/B:JCNS.0000023870.23322.0a.

Kahn, J. A., & Roberts, A. (1982). The neuromuscular basis of rhythmic struggling movements in embryos of *Xenopus laevis*. *Journal of Experimental Biology*, *99*, 197–205.

Kahn, J. A., Roberts, A., & Kashin, S. (1982). The neuromuscular basis of swimming movements in embryos of the amphibian *Xenopus laevis*. *Journal of Experimental Biology*, *99*, 175–184.

Kuehn, C. (2015). *Multiple Time Scale Dynamics* volume 191 of *Applied Mathematical Sciences*. Springer International Publishing. doi:10.1007/978-3-319-12316-5.

Kuznetsov, A. (2004). *Elements of applied bifurcation theory*. Springer Science & Business Media. doi:10.1007/978-1-4757-3978-7.

Li, W.-C., Sautois, B., Roberts, A., & Soffe, S. R. (2007). Reconfiguration of a vertebrate motor network: specific neuron recruitment and context-dependent synaptic plasticity. *The Journal of Neuroscience*, *27*, 12267–12276. doi:10.1523/JNEUROSCI.3694-07.2007.

Liao, G., Diekman, C., & Bose, A. (2020). Entrainment Dynamics of Forced Hierarchical Circadian Systems Revealed by 2-Dimensional Maps. *SIAM J. Appl. Dyn. Syst.*, . URL: https://epubs.siam.org/doi/abs/10.1137/19M1307676.

Mangan, P., Cometa, A., & Friesen, W. (1994). Modulation of swimming behavior in the medicinal leech. IV. Serotonin-induced alteration of synaptic interactions between neurons of the swim circuit. *Journal of comparative physiology. A, Sensory, neural, and behavioral physiology*, *175*, 723–736. doi:10.1007/BF00191844.

Manor, Y., Nadim, F., Abbott, L., & Marder, E. (1997). Temporal dynamics of graded synaptic transmission in the lobster stomatogastric ganglion. *Journal of Neuroscience*, *17*, 5610–5621. doi:10.1523/JNEUROSCI.17-14-05610.1997.

Matveev, V., Bose, A., & Nadim, F. (2007). Capturing the bursting dynamics of a two-cell inhibitory network using a one-dimensional map. *Journal of Computational Neuroscience*, *23*, 169–187. doi:10.1007/s10827-007-0026-x.

Morris, C., & Lecar, H. (1981). Voltage oscillations in the barnacle giant muscle fiber. *Biophysical Journal*, *35*, 193–213. doi:10.1016/S0006-3495(81)84782-0.

Nadim, F., & Manor, Y. (2000). The role of short-term synaptic dynamics in motor control. *Current Opinion in Neurobiology*, *10*, 683–690. doi:10.1016/S0959-4388(00)00159-8.

Nadim, F., Manor, Y., Kopell, N., & Marder, E. (1999). Synaptic depression creates a switch that controls the frequency of an oscillatory cir-

cuit. *Proceedings of the National Academy of Sciences*, *96*, 8206–8211. doi:10.1073/pnas.96.14.8206.

Olenik, M. (2021). PyXPP. https://github.com/markolenik/PyXPP.

Perez, J. M. (1985). Mechanism for global features of chaos in a driven nonlinear oscillator. *Physical Review A*, *32*, 2513–2516. URL: https://doi.org/10.1103/physreva.32.2513. doi:10.1103/physreva.32.2513.

Perkel, D. H., & Mulloney, B. (1974). Motor pattern production in reciprocally inhibitory neurons exhibiting postinhibitory rebound. *Science*, *185*, 181–183. doi:10.1126/science.185.4146.181.

Rabbah, P., & Nadim, F. (2007). Distinct synaptic dynamics of heterogeneous pacemaker neurons in an oscillatory network. *Journal of neurophysiology*, *97*, 2239–2253. doi:10.1152/jn.01161.2006.

Reiss, R. F. (1962). A theory and simulation of rhythmic behavior due to reciprocal inhibition in small nerve nets. In *Proceedings of the May 1-3, 1962, spring joint computer conference* (pp. 171–194). ACM. doi:10.1145/1460833.1460854.

Soffe, S. R. (1993). Two distinct rhythmic motor patterns are driven by common premotor and motor neurons in a simple vertebrate spinal cord. *The Journal of Neuroscience*, *13*, 4456–4469.

Tramontana, F., Gardini, L., Avrutin, V., & Schanz, M. (2012). Period adding in piecewise linear maps with two discontinuities. *International*

Journal of Bifurcation and Chaos, *22*, 1250068. URL: https://doi.org/10.1142/s021812741250068x. doi:10.1142/s021812741250068x.

Tsodyks, M. V., & Markram, H. (1997). The neural code between neocortical pyramidal neurons depends on neurotransmitter release probability. *Proceedings of the National Academy of Sciences*, *94*, 719–723. doi:10.1073/pnas.94.2.719.

Virtanen, P., Gommers, R., Oliphant, T. E., Haberland, M., Reddy, T., Cournapeau, D., Burovski, E., Peterson, P., Weckesser, W., Bright, J., van der Walt, S. J., Brett, M., Wilson, J., Millman, K. J., Mayorov, N., Nelson, A. R. J., Jones, E., Kern, R., Larson, E., Carey, C. J., Polat, İ., Feng, Y., Moore, E. W., VanderPlas, J., Laxalde, D., Perktold, J., Cimrman, R., Henriksen, I., Quintero, E. A., Harris, C. R., Archibald, A. M., Ribeiro, A. H., Pedregosa, F., van Mulbregt, P., & SciPy 1.0 Contributors (2020). SciPy 1.0: Fundamental Algorithms for Scientific Computing in Python. *Nature Methods*, *17*, 261–272. doi:10.1038/s41592-019-0686-2.